A Multifunction Power Converter With Multimode Capabilities for Low Power Electric Vehicles

Virendra Prasad Maurya, *Student Member, IEEE*, and Rajeev Kumar Singh, *Senior Member, IEEE*

***Abstract*—This article proposes a multifunction power converter with multimode capability for the low-power electric vehicle (EV). In multifunction, a single converter provides single-phase on-board charging, motoring, vehicle-to-vehicle (V2V) charging operation, and multiple supplies for EV auxiliaries. In the multimode, the multioutput features of the proposed converter are utilized for functionalities of V2V charging and auxiliary supplies, along with motoring and single-phase charging. Single-phase charging maintains the unity power factor at the source terminal while charging the battery with a constant-current, constant-voltage charging technique and generates three outputs. The first dc (48 V) charges the battery, and two other outputs (12 and 72 V) are used for auxiliary power supply. During the motoring mode also, it generates the three outputs from the 48-V battery. The first ac output drives the brushless dc motor (BLDC) motor by the existing high pulsewidth modulation low-ON switching technique, and the other two outputs (12 and 72 V) cater to the auxiliary power demand of the cabin. The 72-V of the multioutput of the proposed converter is also utilized with V2V charging. The 12-V regulated output eliminates the need for an additional 12-V battery and its charger for the low-power auxiliaries of EVs. Furthermore, the 72-V regulated output decreases the current requirement to feed the high-power auxiliaries. To justify the merits of the proposed converter, multifunction and multimode operation, parameter selection, control algorithm, comparative analysis, loss analysis, and the experimental result with load dynamic are presented in this article. A laboratory scale prototype is developed, which tested 780 W in charging mode, 1000 W in motoring mode, and 480 W during V2V changing operation.**

***Index Terms*—Auxiliary power supply, electric vehicle (EV), multifunction, multioutput, power factor correction (PFC), vehicle-to-vehicle (V2V) charging.**

I. Introduction

AIR pollution is the leading cause of global warming, and the transportation sector is one of its primary sources [1]. Therefore, by adopting electric vehicles (EVs) with new technologies, air pollution can be reduced [2], [3], [4], [5]. The cost of the EVs is a hurdle for their adoption. EVs can be categorized according to the power and distance coverage: 1) high-power long distance, and 2) low-power neighborhood EVs. The high-power EVs need immense energy, so a large battery set is used, increasing the cost [6], [7]. However, an EV for short-distance use, such as within the city, industrial complexes, and golf courts, at low prices can increase EV adoption. There are several low-power, short-distance EVs like Strom R3, Microlino, GEM e4, and Mahindra E20.

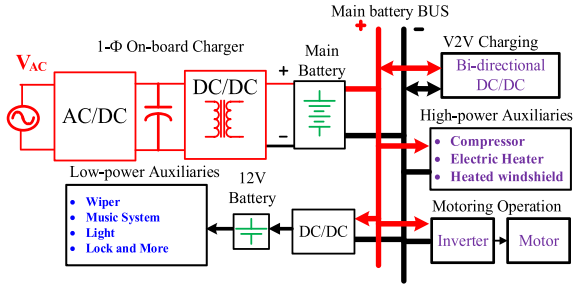

Fig. 1. Conventional EV system.

In EVs, the basic required functions are: 1) on-board charging, 2) V2V charging, 3) motoring operation, and 4) auxiliary power supply, as shown in Fig. 1. Each function requires a specific type of converter. For on-board charging, both ac–dc and dc–dc converters are needed [8], [9]. In motoring mode, a dc–ac inverter is required [10]. Vehicle-to-vehicle (V2V) operation necessitates a bidirectional dc–dc converter, whereas in EVs, a unidirectional dc–dc converter is used to charge the low-power auxiliaries' battery [11], [12].

In [13], [14], [15], and [16], the on-board charger is integrated with a dc–dc converter to charge an auxiliary battery, thus providing only two functionalities. In [13], the on-board charger integrates with a dc–dc converter to charge a low-voltage battery using 20 switches. In [14], the switch count has been reduced from 20 to 18 by integrating the on-board charger with a phase-shift full-bridge converter. In [15], a dual active bridge is used as an on-board charger and is integrated with a phase-shift full-bridge converter comprising 16 switches. However, all the above integrated onboard chargers cannot power the low-power auxiliaries while charging the low-voltage battery. In [16], the auxiliary power module (APM) takes power from the main battery (traction battery) and powers the low-voltage auxiliaries and the 12-V battery simultaneously. This APM is an additional dc–dc converter, which is additionally added along with the on-board charger. This APM uses 16 switches for this operation. In practically low-power EVs like the GEM e4, Arcimoto FUV, and the Mahindra e20, an additional 12-V battery is required, along with a 48-V main battery [17], [18], [19]. The 12-V battery supplies the low-power auxiliaries, and the main battery supplies the high-power auxiliaries, as shown in Table I [20], [21].

Received 13 January 2025; revised 18 March 2025; accepted 16 April 2025. Date of publication 21 April 2025; date of current version 30 June 2025. Recommended for publication by Associate Editor K.-H. Chen. *(Corresponding author: Virendra Prasad Maurya.)*

The authors are with the Department of Electrical Engineering, Indian Institute of Technology (BHU), Varanasi 221005, India (e-mail: virendrapdmaurya.rs.eee19@itbhu.ac.in; rksingh.eee@iitbhu.ac.in).

Color versions of one or more figures in this article are available at https://doi.org/10.1109/TPEL.2025.3562745.

Digital Object Identifier 10.1109/TPEL.2025.3562745

TABLE I
CABIN AUXILIARIES AND ITS SOURCE [20], [21]

Source	Low-power auxiliaries	High-power auxiliaries
12-V battery	Music system, lock, power-steering, wiper and more	--
Main battery (MB)	---	Air compressor, windshield, Electric heater, and more

In [22], [23], and [24], the on-board charger is integrated with the motoring operation and provides only two functionalities. In the integrated circuit of [22], where the interior permanent magnet motor windings have been utilized as the dc–dc inductor in charging operation. For this operation, 14 switches have been used, four of which are used for the mode transformation. Although in [23], 14 switches have been used in the integrated circuit, only one switch is used for mode transformation. However, during the charging operation, the galvanic isolation is missing in the above-integrated circuits [22] and [23]. In [24], the circuit incorporates a coupled magnetic device within the boost converter, allowing it to function either as a boost inductor or an isolated transformer, depending on whether it operates in boost motor drive mode or ac charging mode. However, 24 switches have been used for this operation, in which four switches are used for mode transformation.

In [25] and [26], the on-board charger is integrated with a bidirectional dc–dc converter for V2V charging operation and provides only two functionalities. In [25], an integrated V2V charger is given, where the motor winding neutrals and the negative rails of the on-board drivetrains of both EVs are directly connected. However, access to the motor winding's neutral point is essential for multimode operation, which can increase the machine design complexity. In [26], two on-board chargers are directly connected for the energy transfer between the EVs. However, eight switches have been used for the energy transfer, which can increase the switching losses during the V2V charging.

Overall, the challenges observed in similar prior works are as follows.

1) The existing prior works have the integration of only two functionalities.
2) To power the low-power auxiliaries in EVs, an additional 12-V battery and charger are required.
3) During V2V charging operation, eight switches are used for the energy exchange.
4) In low-power EVs such as Mahindra e2o, the main battery operates at 48 V. If it powers the high-power auxiliaries in EVs, then the current demand tends to be significantly higher compared to high-power EVs where the main battery voltage is more than 400 V.

The proposed power converter provides all four functionalities through a single converter. The block diagram of the proposed idea is shown in Fig. 2. Furthermore, its different functionalities are shown in Fig. 3. The proposed converter integrated with an on-board charger, multioutput for the auxiliary supply, motoring operation, and V2V charging operation, as shown in Fig. 3(a)–(c), respectively. The multioutput features of the proposed converter are utilized for functionalities of

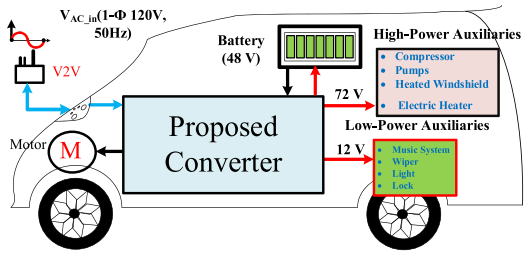

Fig. 2. Block diagram of the proposed converter.

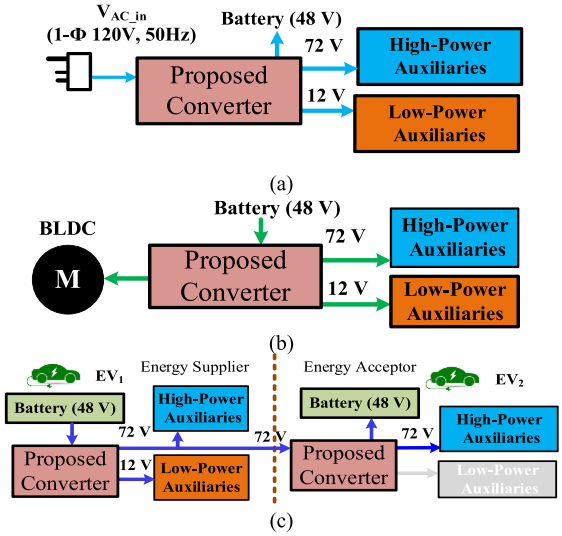

Fig. 3. Multioperation of the proposed converter. (a) 1-Φ charging. (b) Motoring. (c) V2V charging.

V2V charging and auxiliary supplies, along with motoring and single-phase charging.

Contributions of the proposed converter are as follows.

1) It provides multioutputs of 12 and 72 V to cater to the power demand of the EV cabin in all modes of operation. The 12-V battery powers the low-power auxiliaries, and 72-V battery powers the high-power auxiliaries.
2) The 12-V regulated outputs eliminate the requirement of a 12 V battery and its charger, and the 72-V regulated output decreases the current requirement to feed the power to the high-power auxiliaries.
3) It provides a single-phase on-board charger, in which a 120-V, 50-Hz power supply charges the 48-V battery with CC-CV charging technique and maintains the unity power factor (PF) at the source terminal.
4) It provides the motoring operation, in which the brushless dc motor (BLDC) motor is driven with a 48-V battery through an existing high pulsewidth modulation (PWM) low-ON switching technique.
5) It provides V2V charging, in which two proposed power converters from both vehicles are directly connected for energy exchange, and only six switches remain active during this operation.

This article is organized as follows. The detailed operation of the proposed converter in different operating modes is explained

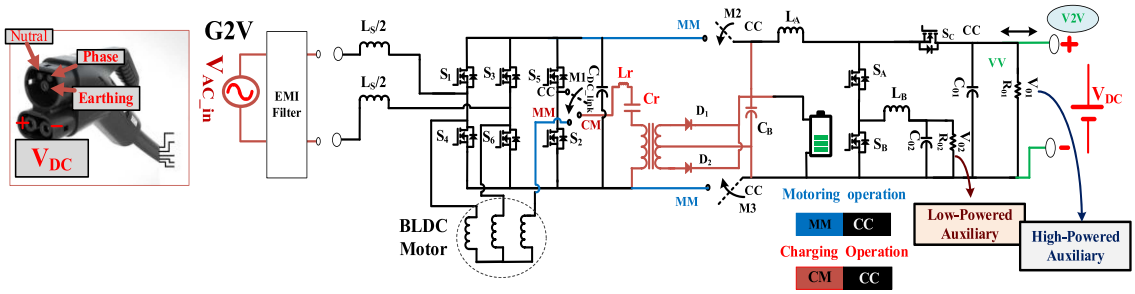

Fig. 4. Circuit diagram of the proposed power converter.

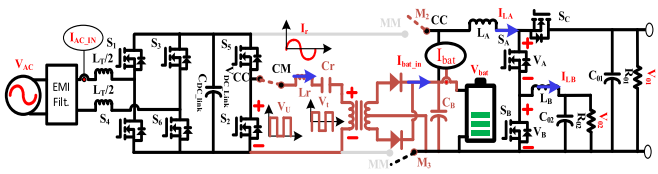

Fig. 5. Proposed converter during ac charging.

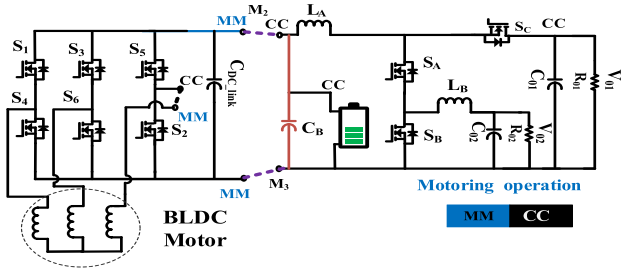

Fig. 6. Proposed converter during motoring operation.

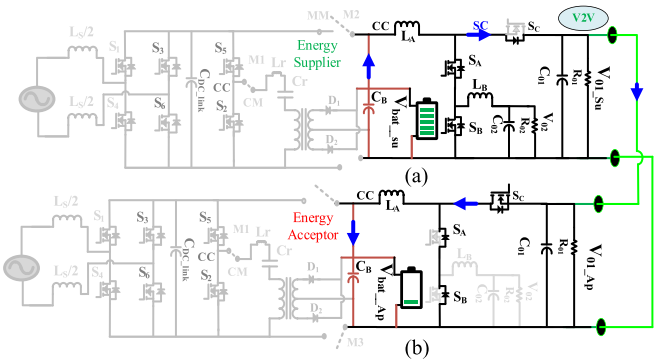

Fig. 7. Connection of the proposed converters for V2V charge transfer, (a) circuit of the energy supplier vehicle, and (b) circuit of the energy acceptor vehicle.

in Section II. Section III presents the design of the circuit parameters. Section IV discusses the control algorithm for the proposed converter. Section V presents the comparative analysis with the existing prior works. The details of the converter's efficiency are explained in Section VI. Section VII presents the experimental validation of the proposed converter, and this article is concluded in Section VIII.

II. Operation of the Proposed Converter

The integrated on-board power converter of multifunctional ties for low-power EVs is shown in Fig. 4. Along with the on-board charging, the different functions are multioutputs in all the modes of operation, motoring operation, and V2V charging.

The multifunction operation is performed with the help of only three switches: M_1, M_2, and M_3. Switch M_1 is a single-pole double-throw switch, and M_2 and M_3 is a single-pole single-through switch. Their single pole terminal is represented by a common mode connection (CC), and the double-through terminals are represented by a charging mode connection (CM) and motoring mode connection (MM). The switch M_1's CC-CM is connected for single-phase charging, and M_2 and M_3 remain open. Furthermore, the power plug is connected at the front end of the proposed converter, as shown in Fig. 5. In motoring mode operation, switch M_1's CC is connected to MM, and the M_2 and M_3 switches CC is connected to the MM connection, as shown in Fig. 6. In V2V operation, all the switches remain open, as shown in Fig. 7. The transition between these modes is conducted at a standstill.

The operation of the proposed converter can be understood by its operation in all the different modes of operation.

A. Single-Phase Charging (M_1, CC-CM)

The proposed converter maintains the unity PF at the source terminal and charges the battery using a constant-current constant-voltage (CC-CV) charging technique. During the charging, it generates three outputs from the single-phase 120-V, 50-Hz power supply. The first dc output of 48 V charges the battery using the CC-CV technique, and the second and third dc outputs of 72 and 12 V meet the power demand of the EV cabin. The steady-state equation of the charging mode is given in the following equations:

The relation between these voltages is stabilized as follows.

$$V_{\text{bat}} = \frac{\sqrt{2} * V_{\text{AC\_in}} |\sin wt| * g_{\text{DC\_}n}}{(1-D) * 2 * n} \tag{1}$$

$$V_{01} = \frac{\sqrt{2} * V_{\text{AC\_in}} |\sin wt| * g_{\text{DC\_}n}}{(1-D) * (1-D_1) * 2 * n} \tag{2}$$

$$V_{02} = V_{01} * D_2 \tag{3}$$

$$g_{\text{DC\_}n} = \left| \frac{{L_n * f_n}^2}{\left[(L_n+1) * {f_n}^2 - 1\right] + j\left[({f_n}^2 - 1) * f_n * Q_L * L_n\right]} \right|$$

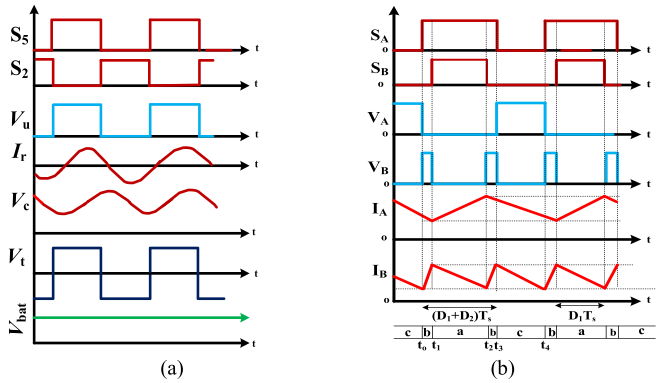

Fig. 8. (a) S_5 and S_2 switching with ZVS operation for charging the battery. (b) S_A and S_B switching for multioutput operation in shoot through (t_2–t_1), power state (t_1–t_0), and zero state (t_4–t_3) in 1-Φ ac charging.

where V_{AC_in} (rms) is source voltage, w is power line angular frequency, D is the duty ratio for switches S_4 and S_6, g_{DC_n} intermediate resonant converter gain, normalized inductance (L_n) is the ratio of magnetizing inductance (L_m) to the leakage inductance (L_r), normalized frequency (f_n) is the ratio of the switching frequency (f_{sw}) of the intermediate switches S_5 and S_2 to the series resonance frequency (f_r) by L_r and C_r, Q_L is the quality factor, and n is the transformer turn ratio. D_1 is the duty ratio of the complete shoot-through interval (t_2-t_1), D_2 is the duty ratio of the power state (t_1-t_0), and the remaining time interval (t_4-t_3) represents the zero state of the converter, as shown in Fig. 8(b).

From the steady state (1), the battery voltage is independent of the multioutput variables. It depends on the gain of the ac supply voltage and duty ratio D of switches S_4 and S_6 and the intermediate converter gain (g_{DC_n}). The ac supply voltage is fixed for the home outlet, and the duty ratio adjusts the dc-link voltage according to the current or voltage at the battery terminal. Furthermore, the value intermediate resonant converter gain (g_{DC_n}) is one for the switching frequency (f_{sw}) equal to the resonance frequency (f_r). It eliminates the additional sensor from the dc–dc conversion in the conventional charging controller. The behavior of the intermediate resonant tank of the proposed converter is explained in Fig. 8(a). It works on series resonance and provides zero-voltage switching (ZVS) in S_5 and S_2 during turn-ON time.

The auxiliary power supply is integrated with the charging operation, and it has two control variables, D_1 and D_2, which are defined in (2) and (3) to regulate the boost and buck auxiliary output voltages. The high-power auxiliary output V_{01} is related to V_{bat} and the D_1 duty ratio of the complete shoot-through. The battery voltage remains constant during charging and discharging operations, and the complete-shoot through duty ratio (D_1) is adjusted according to load variation.

The low-power auxiliary voltage is related to V_{bat}, D_1, and D_2. For a fixed voltage of V_{01}, the effect of D_1 on V_{02} is overcome. D_2 is controlled by V_{02} in any variation in the load. The converter behavior for the multioutput is shown in Fig. 8(b).

B. Motoring Mode (M_1, M_2, M_3 CC-MM)

Switch OFF the single-phase power supply and plug out the single-phase connector. After that, switch M1's CC is connected to MM, and the M_2 and M_3 switches CC is connected to the MM connection to form motoring mode, as shown in Fig. 6. During the motoring operation, it generates three outputs from the battery. The first output drives the BLDC motor using a high-PWM low-ON (HPLN) switching technique, where the PWM width controls its speed, while the second (V_{02}) and third (V_{01}) dc outputs power the low- and high-power auxiliaries of the EV cabin. The HPLN switching also helps in reducing the commutation torque ripple.

The multioutput of the proposed converter remains the same during the motoring mode operation. Only the energy source has been shifted from the single-phase ac supply to the battery.

C. Vehicle-to-Vehicle (V2V) Charging Mode

During V2V charging, all the additional switches, M_1, M_2, and M_3, are turned OFF, and the proposed power converter from both of the vehicles is connected for the energy exchange, as shown in Fig. 7. The steady-state relation between the connected vehicle voltages is given in the following equations:

$$V_{01\_Su} = \frac{V_{bat\_Su}}{(1 - D_{1\_Su})} \tag{4}$$

$$V_{01\_Ap} = V_{01\_Su} \tag{5}$$

$$V_{bat\_Ap} = V_{01\_Ap} * D_C \tag{6}$$

where V_{01_Su} is a supplier boost voltage, V_{bat_Su} is the supplier battery voltage, D_{1_Su} is the supplier complete shoot-through interval, V_{01_Ap} is the acceptor's terminal voltage, V_{bat_Ap} is the acceptor battery voltage, and D_C is the acceptor duty ratio.

The multioutput features of the proposed converter are utilized for functionalities of V2V charging and auxiliary supplies, along with motoring and single-phase charging. Furthermore, the boost output from the auxiliary power supply is also used for the energy transfer and is expressed by (4). The power converter of the energy acceptor extracts the energy from the boost output of the energy supplier terminal, and its voltage expression is given in (5). Furthermore, this voltage is adjusted by switch S_c duty ratio according to the acceptor battery current or voltage requirements, and it is expressed in (6).

III. Selection of the Circuit Parameter for Multimode Operation

The component selection for the integrated on-board power converter of multifunctions is very important. In the selection process of the component, its value is determined in the individual mode of operation. The components are selected based on their maximum tolerance values to ensure proper circuit operation. The selection of components is represented in the sequence of magnetizing inductance, capacitance, resonant tank, and the selection of all the switches.

TABLE II
RATING OF THE SELECTED COMPONENTS

S.N	Eq.	Charging operation	Motoring operation	Selected components
(1)	(7)	$L_{Source} = \frac{{V_{AC}}^2}{\%I_{ripple} * P_o * f_{sw}} \left(1 - \frac{\sqrt{2} * V_{AC}}{V_{DC}}\right)$	Not required	2 mH (DCR=0.74 Ω)
(2)	(8)	$L_A = \frac{V_{bat} * D1}{f_s * \Delta I_A}$	$L_A = \frac{V_{bat} * D1}{f_s * \Delta I_A}$	1 mH (DCR=0.37 Ω)
(3)	(9)	$L_B = \frac{(V_{bat} - V_{02}) * D_2}{f_s * \Delta I_B}$	$L_B = \frac{(V_{bat} - V_{02}) * D_2}{f_s * \Delta I_B}$	0.8 mH (DCR=0.7 Ω)
(4)	(10)	$C_{dc\_link} \geq \frac{2 * P_o * t_{hold}}{{V_o}^2 - {V_{min}}^2}, C_{dc\_link} \geq \frac{P_o}{2 * \pi * f_{line} * \Delta V_o * V_o}$	Used as a filter	3 mF(ESR=1.05 Ω)
(5)	(11)	$C_{01} = \frac{V_{bat} * D1}{f_s * R_{01} * \Delta V_{01}}$	$C_{01} = \frac{V_{bat} * D1}{f_s * R_{01} * \Delta V_{01}}$	470 μF (ESR=0.15 Ω)
(6)	(12)	$C_{02} = \frac{V_{bat} * (1 - D1 - D_2) * D_2}{8 * {f_s}^2 * (1 - D_1) * \Delta V_{02} * L_B}$	$C_{02} = \frac{V_{bat} * (1 - D1 - D_2) * D_2}{8 * {f_s}^2 * (1 - D_1) * \Delta V_{02} * L_B}$	100 μF (ESR=0.1 Ω)
(7)	(13)	$f_r = 1 / 2 * \pi \sqrt{(L_r * C_r)}$	Not required	32 μH, 2 μF
(8)	(14)	All switches and three additional switches (M_1, M_2, and M_3)		650 V, 32 A 450 V, 30 A

V_{ac} is RMS input voltage; $\%R_{ripple}$ is the percentage of inductor ripple current regulation; P_o is maximum steady state power. f_{sw} is switching frequency, V_{bat} is the battery voltage, D_1 and D_2 are the duty ratio of the complete shoot-through and power state, f_s is the switching frequency of S_A and S_B, and ΔI_A, and ΔI_B are the leakage current ripple in inductors L_A and L_B, respectively, and $V_{DC\,link}$ is dc-link voltage. t_{hold} is hold-up time, V_{min} is the minimum voltage to which the output voltage is allowed to drop, f_{line} is the input line frequency, and ΔV_o is the specified voltage ripple. V_{01} is the boost output, and V_{02} is the buck output of the multioutput. ΔV_{01}, and ΔV_{02} are the voltage ripple in the capacitor C_{01} and C_{02}, respectively.

A. Selection of the Magnetizing Inductance

The magnetizing inductances are selected to minimize the current ripple during their respective operating modes. The source inductance is used to minimize the ripple current during charging mode, which helps with power factor correction (PFC). The maximum inductor current ripple determines the rating of the source inductor to ensure that the converter operates in continuous conduction mode. The value of the inductor is calculated from (7), as shown in Table II. To optimize its size, field windings of the BLDC motor have been added.

L_A and L_B inductances are determined by the maximum current ripple limit during complete shoot-through and power state for the multioutput operation. They are expressed in Table II by (8) and (9), respectively.

B. Selection of the Capacitance

Capacitors are selected to minimize the voltage ripple in their respective mode of operation. The dc-link capacitor filters out the voltage ripple during charging mode and reutilizes it to filter out the switching ripple during motoring mode operation. The rating of the dc-link capacitor is determined by hold-up time and voltage ripple limitation. The hold-up time is typically taken as one and a half cycles of power frequency. The greater value of the capacitor should be considered from (10), as shown in Table II.

C_{01} and C_{02} capacitances of the proposed converter are determined by the maximum voltage ripple limiting during complete shoot-through and the zero state for multioutput operation. They are expressed by (11) and (12) in Table II, respectively.

C. Selection of the Component in the Intermediate Resonant Converter

In the intermediate section, switches S_5 and S_2 operate at series resonance and reduce the control complexity for the battery charging. Furthermore, in motoring operation, attached to the front-end switches S_1, S_4, S_3, and S_6 drive the BLDC motor. For the component selection, first, select the resonant frequency and design a transformer with leakage inductance (L_r) that is capable of operating at the rated current, and then the resonant capacitor (C_r) is chosen according to the voltage. The operating resonant frequency of the converter is 20 kHz, and according to that the values of L_r and C_r are shown in (13) of Table II.

D. Selection of All the Switches

The switches S_1, S_3, S_5, S_4, S_6, and S_2 should operate at high voltage and current. The selected switch is IPW60R040CFD7, which can operate at 650 V and 32 A current. The selected diode is RURG8060, which can operate at 80 A, 600 V, and the switch S_A, S_B, and S_C is IPW60R040CFD7, selected according to the future scope for the higher power EVs. M_1, M_2, and M_3 are selected for the effective operation during the voltage and current stress in their respective modes. During charging mode operation, the dc-link voltage (470 $V_{DC\text{-}MAX}$) appears on all these switches. During the motoring mode operation, 30 A (max) is drawn from the battery for driving the BLDC, which goes through these switches. The rating of these selected switches is shown in (14) of Table II.

IV. CONTROL ALGORITHM OF THE PROPOSED CONVERTER

The proposed converter is designed based on the rated power within that, the voltage regulation is unaffected, irrespective of the load variation. All the available voltages have a suitable control system to coordinate the power flow between the different loads. The rated power and the voltage level in their individual mode of operation are represented in Table III. Furthermore, the multimode control algorithm is explained along with multioutput operation. The control logic for all these operations is

TABLE III
SPECIFICATION OF THE POWER LEVEL IN THEIR RESPECTIVE MODE OF OPERATION

Mode of operation	Power IN	Voltage and current rating at load			Output power (watt)
Charging	V_{in} = 120 V, I_{in} = 6.5 A (1-Φ ac source)	V_{bat} = 48 V, I_{bat} = 5.5 A (battery as a load)	V_{01} = 72 V, I_{01} = 5.5 A (high-power auxiliary load)	V_{02} = 12 V, I_{02} = 5 A (low-power auxiliary load)	264+396+60 = 720
Motoring	V_{bat} = 48 V, I_{bat} = 21 A (battery as a source)	V_{BLDC} = 48 V, I_{BLDC} = 10 A (BLDC motor as a load)	V_{01} = 72 V, I_{01} = 5.5 A (high-power auxiliary load)	V_{02} = 12 V, I_{02} = 5 A (low-power auxiliary load)	480+396+60 = 936
V2V	V_{bat} = 48 V, I_{bat} = 10 A (battery as a source)	---	V_{01} = 72 V, I_{01} = 5.5 A (high-power auxiliary load)	V_{02} = 12 V, I_{02} = 5 A (low-power auxiliary load)	396+60 = 456

V_{bat} and I_{bat} (battery voltage and current), V_{01} and I_{01} (high-power auxiliaries' voltage and current), V_{02} and I_{02} (low-power auxiliaries' voltage and current), and V_{BLDC} and I_{BLDC} (motor voltage and current rating).

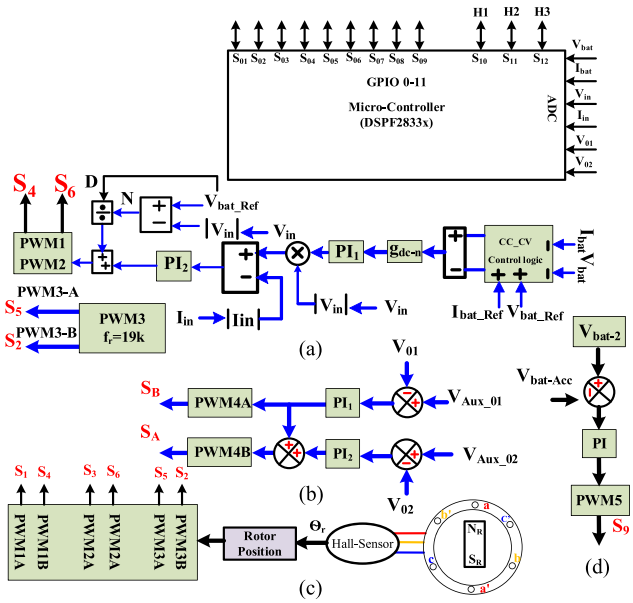

Fig. 9. Control logic of the proposed system for (a) power factor correction, (b) regulated auxiliary power supply voltage, (c) BLDC motor drive operation, and (d) acceptor vehicle control logic.

shown in Fig. 9. Nine sensing parameters have been used for all these operating modes, which are appropriately tuned to prevent unintended control loop behavior. Six sensing perimeters, V_{bat}, I_{bat}, V_{in}, I_{in}, V_{01}, and V_{02}, have been used for charging and the auxiliary power supply, and three sensing parameters of Hall effect sensors H_1, H_2, and H_3 have been used for the motor drive. The modes are selected by the three additional switches, M_1, M_2, and M_3, and the controller is performed according to the selected mode.

A. Control Logic for Single-Phase Charging

Two independent loops have been used in single-phase charging to avoid the coupling effect. The first controller maintains the unity PF at the source terminal and charges the battery with a constant-current constant-voltage technique, as shown in Fig. 9(a). Furthermore, the second controller maintains the regulated auxiliary power supplies to the EV cabin, as shown in Fig. 9(b).

1) Controller I: In the first controller, the outer voltage control (PI_1) and the inner current control (PI_2) work in a cascade, in which one controller acts as the set point for another controller to maintain coordination.

1) *Voltage control loop (PI_1):* Four sensing parameters, V_{bat}, I_{bat}, V_{in}, and I_{in}, are used for CC-CV charging with a unity PF at the source terminal. The CC-CV charging technique is used for the battery's long life [27], [28], [29]. In this charging technique, the battery's 80%–90% state of the charge (SOC) is charged through the CC method, and the remaining SOC of the battery is charged through the CV method. The output of the CC-CV logic is to be an input to the resonant converter. The gain of the resonant converter is one for switching S_5, and S_2 at the nominalized frequency ($f_n = \frac{f_{switching}}{f_{resonance}}$). It also provides ZVS during ON time. Furthermore, the value of the PI_1 controller is determined by the $\frac{\hat{V}_{bat}}{\hat{I}_{in}}$ voltage control transfer function. The bandwidth of this transfer function is 5 Hz, at a phase margin of 60°, which can easily filter out the double-line power frequency but affects the dynamic operation [30]. The digital controller improves the dynamic compensation during load jumps for better output regulation.
2) *Current control loop (PI2):* The controlling parameters of the PI_2 controller are obtained by the $\frac{\hat{i}_{in}}{\hat{D}}$ transfer using small signal analysis for PFC. The bandwidth of the transfer function is kept below or equal to 10% of the switching frequency, and here, it is 2 kHz at a phase margin of 60°, and gain margin (GM) of infinity. The output of the current controller loop's closed-loop duty ratio is added to the feedforward open-loop duty ratio [31]. The generated pulse for the switches S_4 and S_6 by summation of the closed-loop duty and the feedforward open-loop duty charges the dc-link capacitor according to the load at the battery terminal. If the load increases, then the duty ratio increases to increase the charge on it and decreases

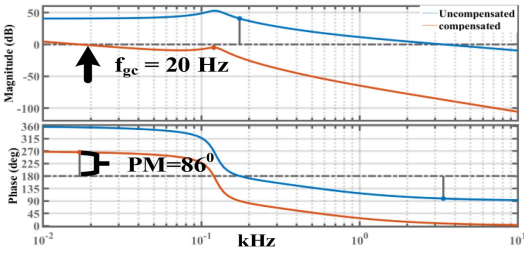

Fig. 10. Bode plot of the uncompensated and compensated high-power auxiliaries' voltage.

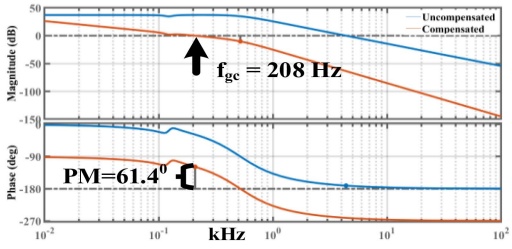

Fig. 11. Bode plot of the uncompensated and compensated low-power auxiliaries' voltage.

with the decrease in the load. This duty ratio generates the pulse for switches S_4 and S_6 to perform PFC and CC-CV charging.

2) Controller II: Controller II is mutually exclusive from Controller I, as shown in Fig. 9(b). Controller II maintains regulated voltages for the high-power and low-power auxiliaries. The error of the high-power auxiliary terminal is corrected by the PI_1 controller, which is tuned by the $\frac{\hat{V}_{01}}{\hat{D}_1}$ transfer function, and the bandwidth is 20 Hz at a phase merging of 86° at the GM of 4.87 dB, as shown in Fig. 10. The PI_1 controller output is added to the PI_2 controller output, which is tuned by the $\frac{\hat{V}_{02}}{\hat{D}_2}$ transfer function, with a bandwidth of 208 Hz, at a phase margin of 61.4° and a GM of 10.2 dB, as shown in Fig. 11. The $\frac{\hat{V}_{01}}{\hat{D}_1}$ and $\frac{\hat{V}_{02}}{\hat{D}_2}$ transfer functions are given in the following equations:

$$\left[\frac{\hat{V}_{01}}{\hat{D}_1}\right]_{\hat{D}_2=0} = \frac{n_3S^3+n_2S^2+n_1S^1+n_o}{S^4+d_3S^3+d_2S^2+d_1S^1+d_o} \tag{15}$$

$$\left[\frac{\hat{V}_{02}}{\hat{D}_2}\right]_{\hat{D}_1=0} = \frac{a_2S^2+a_1S^1+a_o}{S^4+d_3S^3+d_2S^2+d_1S^1+d_o} \tag{16}$$

where $n_3 = -\frac{i_{LA}}{C_{01}}$, $n_2 = \frac{V_{01}(1-D_1)}{L_AC_{01}} - \frac{i_{LA}}{C_{01}C_{02}R_{02}}$, $n_1 = \frac{V_{01}(1-D_1)}{L_AC_{01}C_{02}R_{02}} - \frac{i_{LA}}{C_{01}C_{02}L_B}$, $n_o = \frac{V_{01}(1-D_1)}{L_AL_BC_{01}C_{02}}$, $a_2 = \frac{V_{01}}{L_BC_{02}}$, $a_1 = \frac{V_{01}}{L_BC_{02}C_{01}R_{01}} - \frac{i_{LA}D_2}{L_BC_{01}C_{02}}$, $a_0 = \frac{(1-D_1)^2V_{01}}{L_AL_BC_{01}C_{02}}$, $d_3 = \frac{1}{R_{01}C_{01}} + \frac{1}{R_{02}C_{02}}$, $d_2 = \frac{1}{R_{01}C_{01}R_{02}C_{02}} + \frac{{D_2}^2}{L_BC_{01}} + \frac{1}{L_BC_{02}} + \frac{(1-D_1)^2}{L_AC_{01}}$, $d_1 = \frac{{D_2}^2}{L_BC_{01}C_{02}R_{02}} + \frac{1}{L_BC_{02}C_{01}R_{01}} + \frac{(1-D_1)^2}{L_AC_{01}C_{02}R_{02}}$, $d_0 = \frac{(1-D_1)^2}{L_BL_AC_{01}C_{02}}$

$$\left[\frac{\hat{V}_{\text{bat-acct}}}{\hat{D}_C}\right] = \frac{S^1}{S^2+\frac{S^1}{R_{01}C_{01}}+\frac{1}{L_AC_{01}}}. \tag{17}$$

The output of the PI_1 controller generated a pulse for the switch S_B, and the summation of PI_1 and PI_2 controller outputs generated the pulse for switch S_A.

B. Control Logic for the Motoring Mode Operation

The speed of the BLDC motor is controlled by two main methods: 1) voltage control and 2) PWM control. In voltage control, the speed of the BLDC is directly proportional to the applied voltage. While in the PWM control scheme, the speed of the motor is controlled by the duty cycle of the applied PWM. An increase in turn-ON time raises the average voltage, thereby increasing the motor's speed. Conversely, reducing the turn-ON time of the PWM decreases the motor's speed.

The controller in Fig. 9(c) performs the motoring mode operation, and controller II for the cabin power supply remains active as same as in single-phase charging mode. The speed controller determines the rotor's exact position by the three Hall effect sensors: H_1, H_2, and H_3, and the inverter is excited according to that position to create a revolving field by high-PWM low-ON switching. The high PWM switching in S_1, S_3, and S_5 of the upper leg of the inverter changes the average voltage applied to the motor. The lower switches S_4, S_6, and S_2 are turned on in their respective time intervals [32], [33].

C. Control Logic for the V2V Charging

For V2V charging, the proposed power converter from both of the vehicles is connected. The controller for the energy supplier vehicle remains the same as the auxiliary power supply explained in single-phase charging [see Fig. 9(b)], and the energy acceptor vehicle controller is given in Fig. 9(d). The auxiliary power of the energy supply vehicle is active during energy exchange time. The energy acceptor vehicle controller is designed by the $\frac{\hat{V}_{\text{bat-Ap}}}{\hat{D}_c}$ transfer function is given in (17). The high-power auxiliary voltage of 72 V is buck according to the acceptor vehicle's required battery voltage and charges with the desired current rate.

V. Comparative Analysis of the Proposed Converter

Comparative analysis of the proposed converter is described in two methods: 1) differences in their functioning and their specifications with similar prior work, and 2) cost comparison with them. Comparative analysis with the existing converters is given in Table IV.

Comparative analysis with the existing converter is expressed with multifunction, multimode, and multioutput functions. In [9], the integrated converter provides a wide range of output for the battery charging with three additional switches, with an efficiency of 91%. However, this system requires two additional converters for the basic operation of the EV: one for charging the low-power auxiliary battery and another for driving the motor. In [22], the APM is integrated with the on-board charger and charges the main battery and the LV battery simultaneously. However, 18 switches are used for this operation. Nevertheless, a separate converter is still needed for motoring operations. In [23], the integrated converter performs multifunction operations,

TABLE IV
COMPARATIVE ANALYSIS WITH THE SIMILAR PRIOR WORKS

L.No.	Multifunction (Efficiency)		M-Out	V2V (480 W)	Requirement of Auxiliary Battery & its charger		Function	Galvanic isolation	Switches		Additional Switch for Mode Transfer	Total Switches
	OBC (780 W)	MM (1 kW)			12 V	Charger			MOSFET	Diode		OBC
[9]	✓(91)	×	×	×	✓	✓	**1**	✓	8	12	3	**23**
[22]	✓*	×	✓	×	✓	×	**2**	×	14	4	0	**18**
[23]	✓(89.9)	✓	×	×	✓	✓	**2**	×	6	4	4	**14**
[24]	✓(90)	✓(94)	×	×	✓	✓	**2**	✓	20	0	4	**24**
[25]	✓**	×	×	✓(91.5)	✓	✓	**2**	×	8	0	0	**8**
P.C	✓(91.9)	✓(92.3)	✓	✓(93.2)	×	×	**4**	✓	9	2	3	**14**
L.No.= Literature number, OBC=on-board charger, MM=motoring operation, M-out=multioutput, "✓*" completer on-board charging efficiency not given, "✓**" efficiency is not given,												

TABLE V
COST COMPARATIVE ANALYSIS

S. N	Component	Conventional system				Proposed system	
		MM [23]	CM [23]	V2V [25]	Total (USD)	Com.	Total (USD)
1.	Switch, Diode	6,4		4	10×11+4×4	9,2	9×11+2×4
3.	Gate-driver Accessories	6		4	10×3+10	9,2	9×3+10
2.	Heat-sink	1		1	2×20	1	1×20
4.	12-V Battery	1			32	0	0
5.	12-V Charger	1			10	0	0
6.	PCB	1		1	2×62	1	62
7.	Additional switch	4		0	4×7	3	3×7
Total Cost (in $)					400		247

enabling the on-board charger to charge the main battery with an efficiency of 89.9% and also drives the motor. These functionalities are achieved using 10 switches and four additional switches, but the on-board charger lacks galvanic isolation. In [24], the integrated isolated on-board charger supports both charging and motoring operations with efficiency of 90% and 94%. However, in both [23] and [24], a separate converter is required for low-power auxiliary battery charging.

The above-mentioned converter either performs the multifunction operation or provides the multioutput for charging the additional low-power auxiliary battery.

An additional bidirectional converter is required for V2V charging operation in the above-mentioned converter. In [25], for the multimode operation, the neutral point of the motor winding and the negative rail of the two on-board chargers are connected for V2V charging. It performs V2V charging with an efficiency of 91.5%. However, access to the motor winding's neutral point is essential for multimode operation, which can increase the machine design complexity. However, a higher switch count can increase the switching loss. In the proposed system, only six switches are active while V2V charging.

Furthermore, the cost comparative analysis of the proposed converter is given in Table V. For motoring mode (MM) and charging mode (CM) operation, [23] has been chosen for comparison because it has a minimum number of switches, i.e., 14, amongst prior works for MM and CM mode. Similarly, for comparison in V2V mode, the research presented in [25] has been chosen because it has a minimum number of switches, i.e., four for V2V mode.

Table V presents a cost comparison between the proposed converter with the existing converter. The switches (IPW60R040CFD7), diode (RURG8060), gate driver (FOD3184), heat sink (1960012091T00S), PCB (FR4 epoxy glass), absorbent glass mat battery of 12 V (Mahindra & Mahindra), and relay (V23076-A3001-C132) are the names of the components utilized for this analysis. The suggested solution would set you back 261 USD, whereas the standard converter will set you back 400 USD altogether. The suggested technique saves about USD 159 in costs.

VI. EFFICIENCY ANALYSIS OF THE PROPOSED CONVERTER'S

In power electronics converters, the main losses are switch losses, inductor loss, diode loss, transformer loss, capacitor series resistance loss, inductor direct current loss, and other losses. These losses are represented in Table VI.

A. Loss Analysis of Charging Mode Operation

In charging mode, a total of 12 switches operate in the active state. Among them, eight switches function in hard switching, two diodes experience conduction and switching losses, and two switches operate under ZVS. Other losses are transformer loss, multioutput converter loss, and other losses like EMI and EMC loss. The converter operating power is shown in Table VII. Furthermore, their loss distribution is shown in Fig. 12.

Efficiency of the proposed converter during charging mode is $= (780-63.29)/780 = 0.9188 = 91.88\%$

B. Loss Analysis of Motoring Mode Operation

In motoring mode, a total of 12 switches are operated. The front six switches, i.e., S1, S2, S3, S4, S5, and S6, are operated with high-PWM low-ON switching. The dc-link capacitor of the charging mode operates as a filter capacitor in motoring mode, which produces capacitor equivalent series resistance

TABLE VI
FORMULATION OF THE BASIC POWER ELECTRONICS CONVERTER LOSSES

Elements	Losses
Switch loss	$P_{sw}=\frac{V_{in}I_{in}\left(t_r+t_f\right)f_{sw}}{2}, P_c = R_{DS(ON)} * I_{in}{}^2(\text{rms})$
Inductor loss	$P_{ind} = DCR * I_{in}{}^2(\text{rms})$
Diode loss	$P_{D(cond)} = V_f * I_f, P_{D(rev.lek)} = V_r * I_r, P_{D-sw} = \frac{V_f I_f\left(t_r\right)f_{sw}}{2}$
Transformer loss	$P_{T(cond)} = I_{in}{}^2(\text{rms})* R_{Turn}, P_h = \eta * B_{max}{}^n f * V$ $P_{eddy} = K_e * B_{max}{}^2 * f^2 * t^2 * V$
Capacitor loss	$P_{C-L} = ESR * I_{in}{}^2(\text{rms})$
Gate driver loss	$P_{\text{gate}}= Q_g * V_{\text{gate}} * f_{\text{sw}}, P_{\text{static}}=V_{DC} * I_q$

Where: P_{sw} (switching losses), V_{in} (input voltage), I_{in} (input current), t_r (rise time), t_f (fall time), f_{sw} (switching frequency), P_c (switch conduction loss), R_{DS} (swich conducting resistance), P_{ind} (inductor loss), DCR (inductor direct current resistance), $P_{D(cond)}$ (diode forward conduction loss), $P_{D(rev.lek)}$ (diode revers conduction loss), $P_{D\text{-}SW}$ (diode switching loss), $P_{T(cond)}$ (transformer conduction loss), P_h (transformer hysteresis loss), P_{eddy} (transformer eddy current loss), ESR (capacitor equivalent series resistance). P_{gate} (gate charge energy consumption), Q_g (gate charge), V_{gate}(driver turn-on votlage), P_{static} (static power consumption in gate driver), V_{DC} (supply voltage of the gate driver), I_q (quiescent current).

TABLE VII
LOSS DURING SINGLE-PHASE CHARGING OPERATION

Loss distribution	Single-phase charging (780 W)
Front end converter	15.34
Resonant tank	2.13
Transformer	0.832
Multioutput	33.6
Other loss	11.19
Total loss	63.29
Output power	716

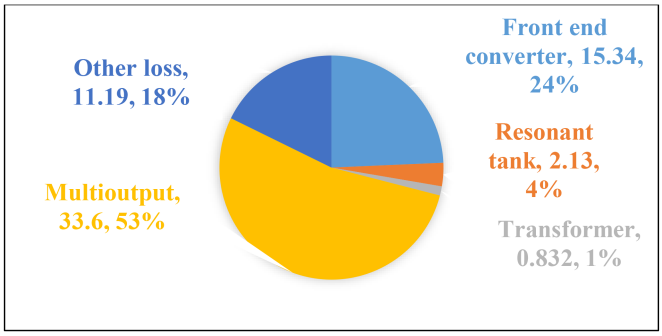

Fig. 12. Map of the proposed converter loss distribution during charging mode.

conduction loss, multioutput converter loss, and other losses are EMI and EMC, etc. The operating power and its respective losses are listed in Table VIII. Furthermore, their loss distribution is shown in Fig. 13.

Efficiency of the proposed converter during motoring mode operation is = (1000–76.44)/1000 = 0.923 = 92.3%

TABLE VIII
LOSS DURING MOTORING MODE (MM) OPERATION

Loss Distribution	MM (1000 W)
Switching	28.24
Filter	3.95
Multioutput	33.6
Other loss	10.65
Total losses	76.44
Power used	923.55

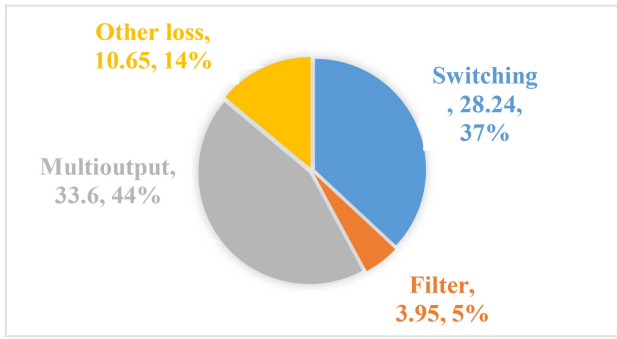

Fig. 13. Map of the proposed converter loss distribution during motoring mode.

TABLE IX
PROPOSED CONVERTER LOSS DURING V2V CHARGING

Loss distribution	V2V (480 W)
S_A	17.12
S_B	9.28
L_{A+B}	1.18
C_{01+02}	0.52
S_C	4.21
Other loss	1.28
Total loss	33.59
Output power	446.4

C. Loss Analysis of V2V Charging Mode

For V2V charging, the proposed power converter from both of the vehicles is directly connected, and only six switches remain in active state. For the efficiency analysis, only the energy supplier vehicle is considered. The loss analysis is determined by the switching loss in S_A and S_B switches with one diode, and the filer capacitor and the inductor loss with the other loss are considered. During V2V operation, the operating power and its operational losses are listed in Table IX. Furthermore, the loss distribution during V2V operation is expressed in Fig. 14.

Efficiency of the proposed converter during V2V charging = (480−33.6)/480 = 0.93 = 93%

The loss analysis of the proposed converter is expressed through the pie chart in their individual mode of operation. In this efficiency analysis, the new analysis is added with the previous because previously loss is given at a particular load, but now efficiency is taken by varying the load from 10% to 100%. An

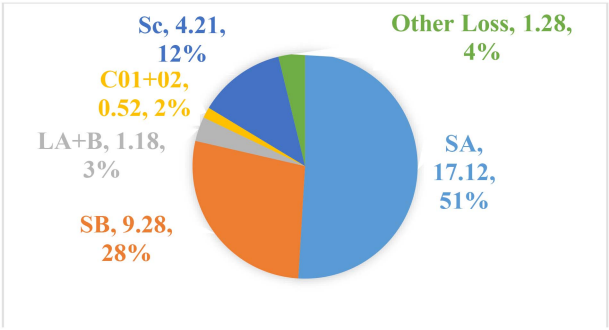

Fig. 14. Map of the proposed converter loss distribution during V2V charging.

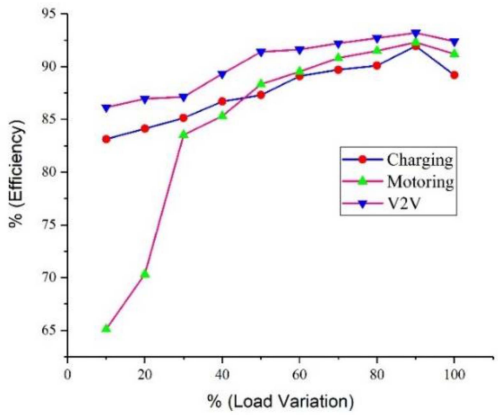

Fig. 15. Efficiency curve of all the modes of operation.

efficiency graph of the proposed power converter is given in Fig. 15.

VII. Experimental Validation

The experimental result of the proposed converter is expressed with integrated on-board chargers with their different functionalities. In its multifunction, it performs single-phase charging, motoring, V2V charging, and multioutput. The multioutput features of the proposed converter are utilized for functionalities of V2V charging and auxiliary supplies, along with motoring and single-phase charging. The pictorial representation of the proposed converter is shown in Fig. 16.

A. Multifunction Operation of the Proposed Converter

1) Charging Operation With the Auxiliary Power Supply: In charging operation, it maintains the unity PF at the source terminal and charges the battery from the 120 V, 50 Hz single-phase power supply. During the charging, it generates three outputs; the first dc output charges the 48-V battery, and the second and third outputs of 12 V (V_{02}) and 72 V (V_{01}) meet the power demand of the cabin.

a) UPF with multioutput during charging operation: According to the industry standard IEC61000-3-2, during single-phase charging, the PF should be greater than 0.98. During the single-phase ac charging, source voltage and current are in phase with 0.99 PF, and the multioutputs are shown in Fig. 17.

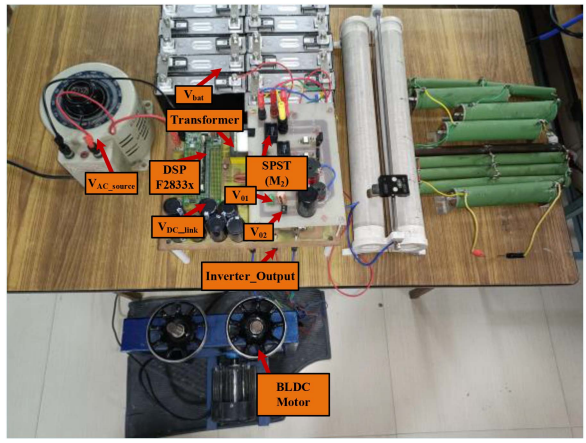

Fig. 16. Photograph of an experimental prototype of the proposed converter.

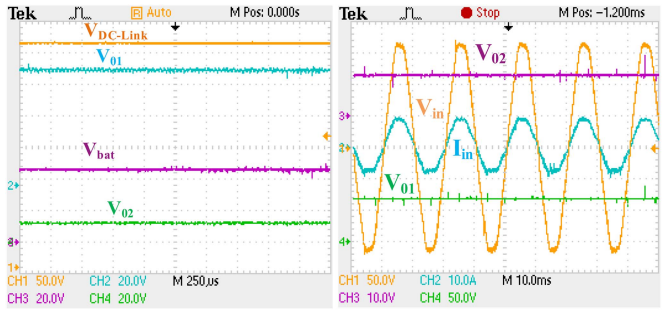

Fig. 17. During ac charging (a) available output voltages for battery and cabin's power demand and (b) unity power factor with the auxiliaries' voltages.

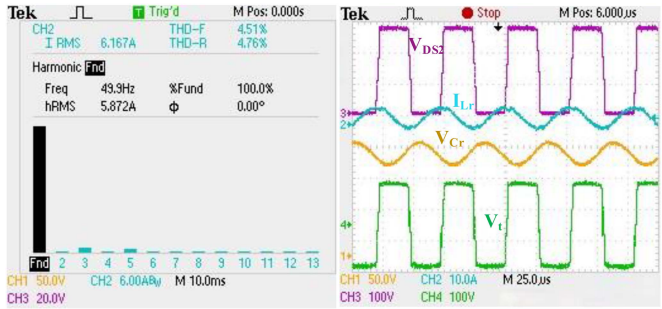

Fig. 18. (a) THD spectrum of the source current and (b) intermediate resonant converter operation during series resonance.

DC-link voltage ($V_{\text{CD-Link}}$), battery voltage (V_{bat}), and the available auxiliary voltages V_{01} and V_{02} are shown in Fig. 17(a). Furthermore, the single-phase ac power supply source voltage (V_{IN}) is in phase with the source current (I_{in}), and the auxiliary voltages (V_{01} and V_{02}) for the power support of the EV cabin are shown in Fig. 17(b).

b) THD spectrum of the source current and operation of the intermediate resonant converter: The amplitude of the source current, with their respective harmonics, is shown in Fig. 18(a). According to the IEEE 519-2014, the total harmonic distortion (THD) value should be less than 5% [34]. The THD as

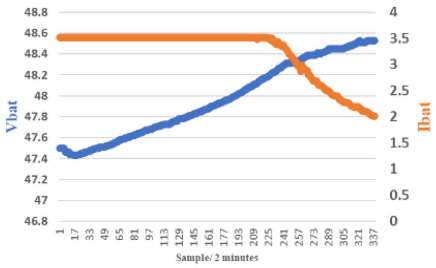

Fig. 19. CC-CV charging operation.

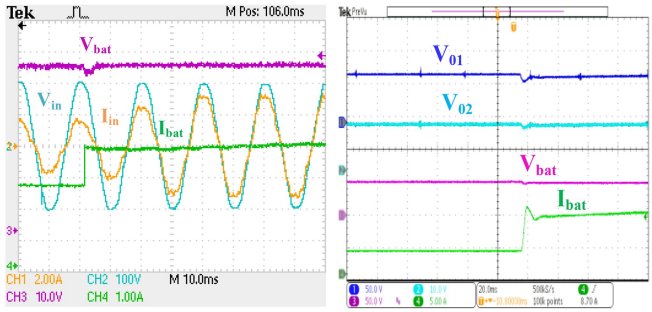

(a) (b)

Fig. 20. In single-phase charging (a) power factor at the source terminal is maintained during load dynamics and (b) available voltage is sustained after load dynamics is applied at high-power auxiliary.

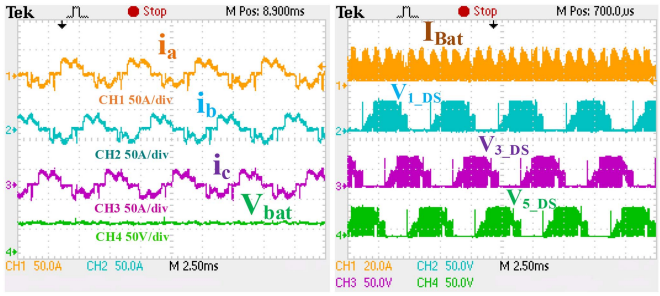

(a) (b)

Fig. 21. (a) Motor line currents i_a, i_b, and i_c with battery voltage. (b) Battery input current with voltage across the switch (V_{DS}).

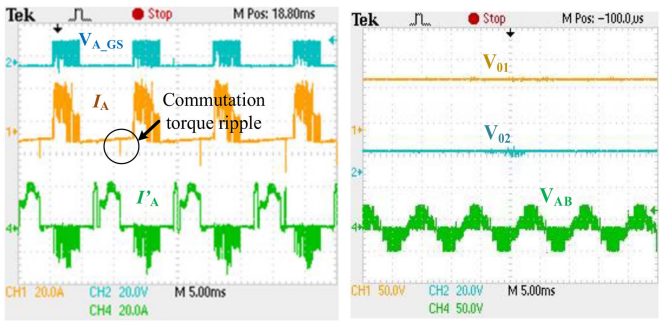

(a) (b)

Fig. 22. (a) Inverter switch current of one leg when driven with high pulsewidth modulation low-ON switching scheme. (b) Multioutput with line voltage (V_{AB}) during motoring operation.

a percentage of the root mean square value of the source current is 4.76%, and the percentage of the fundamental RMS value of the source current is 4.51%.

The resonant tank of the proposed converter works at a normalized frequency and provides unity gain with ZVS during turn-ON time while single-phase charging. During the resonance, sinusoidal current (I_{Lr}) flows through the circuit, and unipolar (V_U) and bipolar voltage (V_t) appear at the switch S_2 and the transformer terminal, respectively, as shown in Fig. 18(b).

c) CC-CV charging technique: A graph plotted between battery voltage and current data, which is taken every 2 min, is shown in Fig. 19. The constant current 3.5 A charges the 48-V battery until the set point of the CC to CV transition. After the set point of 48.2 V, the constant voltage is applied for the remaining SOC, and the current starts to fall.

d) Voltage regulation of charging mode during load dynamic: For the dynamic analysis of the proposed converter during charging mode, a load dynamic is applied at the auxiliary terminal voltages, and the converter performance is analyzed, as shown in Fig. 20. Fig. 20(a) represents that the proposed converter maintains the unity PF at the source terminal, irrespective of a load variation. V_{in} and I_{in} represent the input current and voltage, and V_{bat} and I_{bat} represent the battery voltage and current during load dynamics in on-board charging. Fig. 20(b) shows the voltage regulation of available output voltages of the proposed power converter during on-board charging, irrespective of the variation of the load.

2) Motoring Mode Operation With the Auxiliary Power Supply: In motoring mode, the proposed converter restructures itself and drives the brushless dc motor from the 48-V main battery.

During this operation, it also generates two more outputs, voltages 12 V (V_{02}) and 72 V (V_{01}), for the power support of the EV cabin.

a) Motor current during the load torque: The motor is driven with the battery using an existing HPLN switching scheme, where the upper leg is driven with PWM, and the lower leg is driven with 120° ON. Fig. 21(a) represents the motor line current I_a, I_b, and I_c with battery voltage during its loading condition, and Fig. 21(b) represents the input current of the inverter with a drain to source switching voltage of the upper leg of the inverter. These voltages are V_{A_DS}, V_{B_DS}, and V_{C_DS}, which are 120° phase apart from each other.

b) Commutation torque ripple elimination and auxiliary power supply during motoring operation: The inverter phase-A and upper and lower leg switch currents with its switching are represented in Fig. 22(a) by I_A, I'_A, and $V_{A\text{-}GS}$, respectively. The commutation current ripple from the lower switch current I'_A is greatly minimized. In a similar way, the commutation current ripple from the inverter lower switch currents I'_B and I'_C is also minimized.

Multioutput voltages during motoring operation are shown in Fig. 22(b). In this process, a 72-V (V_{01}) and 12-V (V_{02}) output are generated from a 48-V battery for the auxiliary power supply. The line voltage V_{AB} during the motoring operation is also shown in that one.

c) Voltage regulation of motoring mode during load dynamic: The operation of the proposed converter in motoring

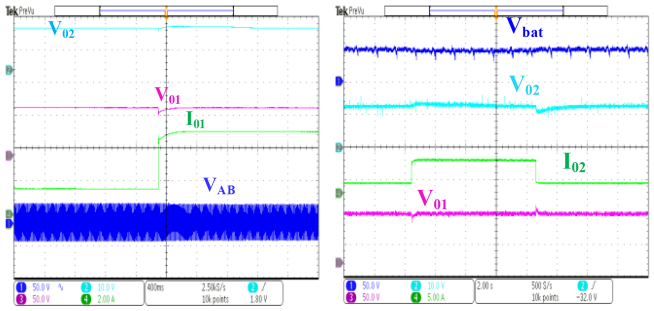

(a) (b)

Fig. 23. Load dynamic during motoring mode. (a) Load dynamic at high-power auxiliaries. (b) Load dynamic at the low-power auxiliaries.

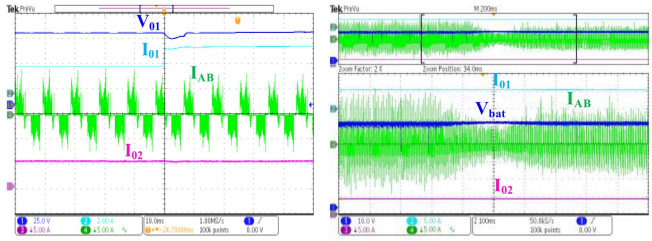

(a) (b)

Fig. 24. Dynamic result of the proposed converter during motoring mode. (a) Load dynamic in high-power auxiliaries. (b) Change in the speed of the motor.

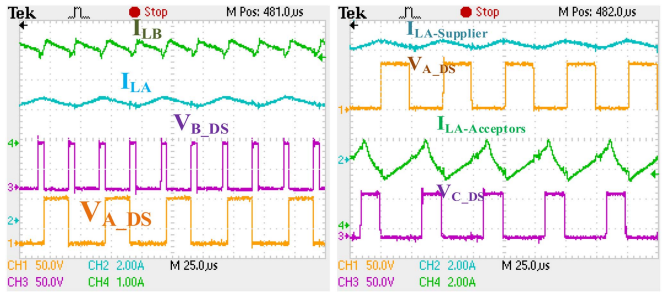

(a) (b)

Fig. 25. (a) Inductors L_A and L_B flux balance with respect to drain to source voltage of switch S_A and S_B, during multioutput and (b) S_A and S_C switching voltages $V_{A\text{-}DS}$, $V_{C\text{-}DS}$, and according to them, the inductor LA's currents $I_{LA\text{-}Supplier}$ and $I_{LA\text{-}Acceptor}$, charging–discharging cycle during V2V charging.

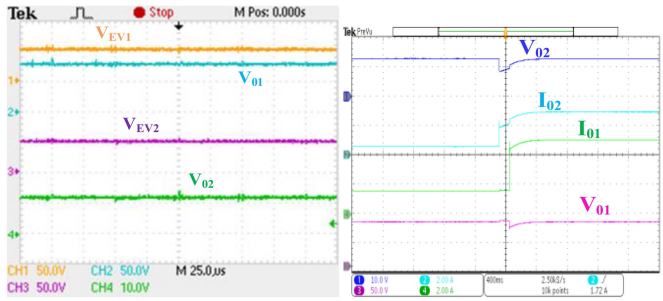

(a) (b)

Fig. 26. V2V operation of the proposed converter. (a) Available voltages during V2V charging. (b) Simultaneously applied the load dynamics in the low-power and high-power auxiliaries.

mode is analyzed by applying load dynamics in high-power and low-power auxiliaries, as shown in Fig. 23. Fig. 23(a) shows the behavior of the high-power auxiliary voltage, low-power auxiliary voltage, inverter line voltages (V_{01}, V_{02}, V_{AB}), and the high-power auxiliary load current (I_{01}) during the application of a dynamic load to the high-power auxiliary system. Furthermore, a load dynamic applied at the low-power auxiliary and the converter response is shown in Fig. 23(b), where V_{bat}, V_{01}, V_{02}, and I_{02} represent the battery voltage, high-power auxiliary voltage, low-power auxiliary voltage, and current, respectively.

The BLDC motor and auxiliary loads are connected in parallel, and their operations are independent of each other. If the auxiliary power varies, then that power is not reflected in the motor operation, as shown in Fig. 24(a). Furthermore, the speed variation is applied to the BLDC motor, and it does not reflect any current variation of the low-power and the high-power auxiliaries of the cabin, as shown in Fig. 24(b).

3) V2V Charging Operation With the Auxiliary Power Supply: In multimode operation, the proposed power converters from both vehicles are connected to facilitate battery charging through a V2V connection. The boost multioutput feature of the proposed converter is utilized for efficient V2V charging.

a) Multioutput operation of the proposed converter: The proposed converter switching operation during multioutput operation is shown in Fig. 25(a). where I_{LA} and I_{LB} represent the current profile of the inductors L_A, and L_B, and $V_{A\text{-}DS}$ and $V_{B\text{-}DS}$ represent the load voltage across switches S_A and S_B.

b) V2V charging operation: During the V2V charging operation, the current profile of inductor L_A of the energy supplier EV, with switch voltage V_{A_CD} across the switch S_A, and the current profile of inductor L_A of the energy acceptor EV with switch voltage V_{C_DS} across the switch S_C are shown in Fig. 25(b).

i) Available output voltages during V2V charging: Available voltages during V2V charging operation are shown in Fig. 26(a), where V_{EV1}, V_{01}, and V_{02} represent the battery voltage and high-power and low-power auxiliary voltages of the energy supplier vehicle, and V_{EV2} represents the battery voltage of the energy acceptor vehicle.

ii) Load dynamic during V2V charging mode of operation: To verify the voltage regulation during V2V operation, a simultaneous load is applied at the low-power and high-power auxiliaries, as shown in Fig. 26(b). V_{01} and V_{02} represent the set auxiliaries' voltages, and I_{01} and I_{02} represent the corresponding load current during V2V charging. Both 72- and 12-V loads are connected in parallel and made independent of each other with the help of a control scheme. If the load is applied to the low-power auxiliary voltage (12 V), then there is no influence of the load connected to the high-power auxiliary voltage (72 V), as shown in Fig. 27(a). Furthermore, if the load change is applied at the 72-V terminal, then there is no impact on the 12-V auxiliary supply, as shown in Fig. 27(b). Furthermore, according to the battery chemistry, the rate of charge is adjusted with the help of the controller.

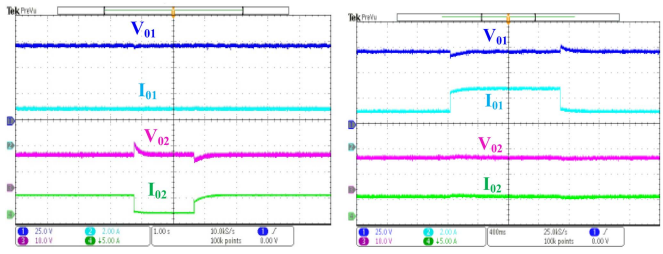

(a) (b)

Fig. 27. Current sharing between 72 and 12 V during different load conditions. (a) Current sharing of high-power auxiliaries unaffected by variation in a load of low-power auxiliaries. (b) Current sharing of low-power auxiliaries unaffected by variation in a load of high-power auxiliaries.

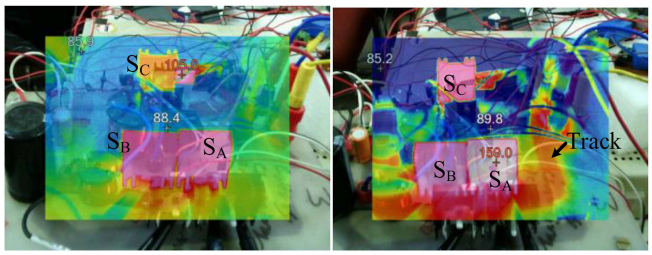

(a) (b)

Fig. 28. Thermal image of the proposed converter. (a) Starting of the converter. (b) After half an hour of the converter's operation.

4) Thermal Profile of the Proposed Converter: In all modes of operation, the switching area has been identified as the primary hotspot in the converter. This finding is validated by the thermal image analysis of the proposed converter, as shown in Fig. 28. These thermal images are taken in two stages of the converter in the initial stage after just starting the operation of the converter, as shown in Fig. 28(a). The main hot spot of the converter is the switches, whose temperature is 105°F (40 °C). After 30 min, this temperature increases by 159°F (70 °C), as shown in Fig. 28(b).

VIII. Conclusion

A multifunction power converter with multimode capabilities has been proposed in this work for low-power EVs. The proposed single converter serves for single-phase on-board charging, multioutput for the auxiliaries, motoring operation, and V2V charging operation. The proposed converter uses 14 switches which is a smaller number of switches with respect to the number of functions compared with similar prior converters. The multioutput features of the proposed converter are utilized for functionalities of V2V charging and auxiliary supplies, along with motoring and single-phase charging. In single-phase charging mode, it charges the 48-V battery from the 120 V, 50 Hz power supply and generates two more outputs of 12 and 72 V to supply the low-power and high-power auxiliaries of the EV cabin. In motoring mode, it drives the BLDC motor with the existing high-PWM low-ON switching technique and generates two additional outputs (12 and 72 V) from the 48-V battery. The multioutput features of the proposed converter are utilized as a V2V charging along with the cabin power demand. The 12-V regulated output eliminates the additional demand for the 12-V battery and its charger. Furthermore, the 72-V regulated output decreases the current requirement to feed the high-power auxiliaries. To express the novelty, a comparative and cost analysis with existing prior works is given in this article. To justify the proposed idea of its multifunction and multimode operation, parameter selection, control algorithm, and loss analysis, the experimental result with load dynamic is presented. The converter's efficiency in single-phase on-board charging, motoring operation, and V2V charging modes are 91.88%, 92.3%, and 93%, respectively, nearly 90% of its rated load. Furthermore, the thermal analysis of the proposed converter is added in the experimental section. A laboratory scale prototype was developed, which tested 780 W in charging mode, 1000 W in motoring mode, and 480 W during V2V changing operation.

References

[1] T. Wu, X. Wei, X. Zhang, G. Wang, J. Qiu, and S. Xia, "Carbon-oriented expansion planning of integrated electricity-natural gas systems with EV fast-charging stations," *IEEE Trans. Transport. Electrific.*, vol. 8, no. 2, pp. 2797–2809, Jun. 2022.

[2] N. Yang, L. Han, C. Xiang, H. Liu, T. Ma, and S. Ruan, "Real-time energy management for a hybrid electric vehicle based on heuristic search," *IEEE Trans. Veh. Technol.*, vol. 71, no. 12, pp. 12635–12647, Dec. 2022.

[3] F. Ju, N. Murgovski, W. Zhuang, Q. Wang, and L. Wang, "Predictive cruise controller for electric vehicle to save energy and extend battery lifetime," *IEEE Trans. Veh. Technol.*, vol. 72, no. 1, pp. 469–482, Jan. 2023.

[4] A. Choudhary, S. Fatima, and B. K. Panigrahi, "State-of-the-art technologies in fault diagnosis of electric vehicles: A component-based review," *IEEE Trans. Transport. Electrific.*, vol. 9, no. 2, pp. 2324–2347, Jun. 2023.

[5] A. Sierra, C. Gercek, K. Geurs, and A. Reinders, "Technical, financial, and environmental feasibility analysis of photovoltaic EV charging stations with energy storage in China and the United States," *IEEE J. Photovolt.*, vol. 10, no. 6, pp. 1892–1899, Nov. 2020.

[6] A. Babin, N. Rizoug, T. Mesbahi, D. Boscher, Z. Hamdoun, and C. Larouci, "Total cost of ownership improvement of commercial electric vehicles using battery sizing and intelligent charge method," *IEEE Trans. Ind. Appl.*, vol. 54, no. 2, pp. 1691–1700, Mar./Apr. 2018.

[7] A. Ostadi and M. Kazerani, "Optimal sizing of the battery unit in a plug-in electric vehicle," *IEEE Trans. Veh. Technol.*, vol. 63, no. 7, pp. 3077–3084, Sep. 2014.

[8] A. Singh, J. Gupta, and B. Singh, "Design and control of two stage battery charger for low voltage electric vehicles using high gain buck-boost PFC ac-dc converter," *IEEE Trans. Ind. Appl.*, vol. 59, no. 5, pp. 6125–6135, Sep./Oct. 2023.

[9] B. O. Aarninkhof, D. Lyu, T. B. Soeiro, and P. Bauer, "A reconfigurable two-stage 11 kW dc–dc resonant converter for EV charging with a 150–1000 V output voltage range," *IEEE Trans. Transport. Electrific.*, vol. 10, no. 1, pp. 509–522, Mar. 2024.

[10] X. Chen and G. Liu, "Sensorless optimal commutation steady speed control method for a nonideal back-EMF BLDC motor drive system including buck converter," *IEEE Trans. Ind. Electron.*, vol. 67, no. 7, pp. 6147–6157, Jul. 2020.

[11] E. Ucer et al., "Analysis, design, and comparison of V2V chargers for flexible grid integration," *IEEE Trans. Ind. Appl.*, vol. 57, no. 4, pp. 4143–4154, Jul./Aug. 2021.

[12] C. Wang, P. Zheng, and J. Bauman, "A review of electric vehicle auxiliary power modules: Challenges, topologies, and future trends," *IEEE Trans. Power Electron.*, vol. 38, no. 9, pp. 11233–11244, Sep. 2023.

[13] Y.-S. Kim, C.-Y. Oh, W.-Y. Sung, and B. K. Lee, "Topology and control scheme of OBC–LDC integrated power unit for electric vehicles," *IEEE Trans. Power Electron.*, vol. 32, no. 3, pp. 1731–1743, Mar. 2017.

[14] G. Yu and S. Choi, "An effective integration of APM and OBC with simultaneous operation and entire ZVS range for electric vehicle," *IEEE Trans. Power Electron.*, vol. 36, no. 9, pp. 10343–10354, Sep. 2021.

[15] I. Kougioulis, A. Pal, P. Wheeler, and M. R. Ahmed, "An isolated multiport DC–DC converter for integrated electric vehicle on-board charger," *IEEE J. Emerg. Sel. Topics Power Electron.*, vol. 11, no. 4, pp. 4178–4198, Aug. 2023.
[16] L. Zhu, H. Bai, A. Brown, and M. McAmmond, "Design a 400 V–12 V 6 kW bidirectional auxiliary power module for electric or autonomous vehicles with fast precharge dynamics and zero dc-bias current," *IEEE Trans. Power Electron.*, vol. 36, no. 5, pp. 5323–5335, May 2021.
[17] GW WAEV LLC, "GEM Owner's Manual," 9941150-EN, Rev 01, 2023. [Online]. Available: https://www.gemcar.com/wp-content/uploads/2023/02/9941150.pdf
[18] Arcimoto, "2022 arcimoto FUV owner's manual," P10001 Rev 0, 2022. [Online]. Available: https://drive.google.com/file/d/17ZpgXxqKIwTM5sjuOGhBuiTeIqHgqY4S/view
[19] Mahindra, "e20 Owner's Manual, Rev R0, 2016. [Online]. Available: https://www.scribd.com/document/446289916/Mahindra-Reva-owner-manual
[20] Tata Motors, "Nexon EV Owner's Manual," R24, Jul. 2021. [Online]. Available: https://riyatata.com/assets/images/Nexon-EV-Owner-Manual.pdf
[21] Mitsubishi Motors Corporation, "12MY i-MiEV Owner's Manual," 2012. [Online]. Available: https://mitsubishi-motors.co.uk/wp-content/uploads/2021/06/12MY-i-MiEV-Owners-Manual.pdf
[22] Y. Xiao, C. Liu, and F. Yu, "An integrated on-board EV charger with safe charging operation for three-phase IPM motor," *IEEE Trans. Ind. Electron.*, vol. 66, no. 10, pp. 7551–7560, Oct. 2019.
[23] J. Cai and X. Zhao, "An on-board charger integrated power converter for EV switched reluctance motor drives," *IEEE Trans. Ind. Electron.*, vol. 68, no. 5, pp. 3683–3692, May 2021.
[24] G. T. Chiang, T. Shuji, S. Takahide, Y. Hand, Y. Kitamura, and M. Fukada, "Coupled magnetic-based integrated isolated onboard battery charger and boost motor drive unit for electric vehicles," *IEEE Trans. Transport. Electrific.*, vol. 8, no. 1, pp. 135–148, Mar. 2022.
[25] U. B S, V. Khadkikar, H. H. Zeineldin, S. Singh, H. Otrok, and R. Mizouni, "Direct electric vehicle to vehicle (V2V) power transfer using on-board drivetrain and motor windings," *IEEE Trans. Ind. Electron.*, vol. 69, no. 11, pp. 10765–10775, Nov. 2022.
[26] A. Shafiqurrahman, B. S. Umesh, N. A. Sayari, and V. Khadkikar, "Electric vehicle-to-vehicle energy transfer using on-board converters," *IEEE Trans. Transport. Electrific.*, vol. 9, no. 1, pp. 1263–1272, Mar. 2023.
[27] X. Li, H. Ma, S. Ren, J. Yi, S. Lu, and Q. Feng, "A novel LCL resonant converter with inherent CC-CV output for on-board chargers of plug-in electric vehicles," *IEEE Trans. Power Electron.*, vol. 38, no. 4, pp. 4212–4217, Apr. 2023.
[28] Y. Xu, X. Ge, R. Guo, and W. Shen, "Online soft short-circuit diagnosis of electric vehicle li-ion batteries based on constant voltage charging current," *IEEE Trans. Transport. Electrific.*, vol. 9, no. 2, pp. 2618–2627, Jun. 2023.
[29] W. Xiong, Z. Yan, D. Tang, W. Zhou, and R. Mai, "A hybrid topology IPT system with partial power processing for CC-CV charging," *IEEE Trans. Power Electron.*, vol. 39, no. 1, pp. 1701–1712, Jan. 2024.
[30] R. Valascho and S. Abdel-Rahman, "Digital PFC CCM boost converter - 300 W design example using XMC1400 microcontroller," 2016. [Online]. Available: www.infineon.com
[31] S. Kim and P. N. Enjeti, "Control of multiple single-phase PFC modules with a single low-cost DSP," *IEEE Trans. Ind. Appl.*, vol. 39, no. 5, pp. 1379–1385, Sep./Oct. 2003.
[32] R. A. Raj, D. S. Nair, S. M P, and S. George, "A novel high-voltage gain circuit topology for commutation torque ripple reduction," *IEEE Trans. Ind. Appl.*, vol. 58, no. 5, pp. 6227–6236, Sep./Oct. 2022.
[33] S. Singh, N. B. Y. Gorla, K. Jayaraman, and J. Pou, "Analysis and mitigation of common-mode noise with different modulation strategies in SiC-fed three-phase brushless DC motor drive," *IEEE J. Emerg. Sel. Topics Power Electron.*, vol. 12, no. 1, pp. 663–674, Feb. 2024.
[34] B. Zhang, S. Xie, Z. Li, P. Zhao, and J. Xu, "An optimized single-stage isolated swiss-type AC/DC converter based on single full-bridge with midpoint-clamper," *IEEE Trans. Power Electron.*, vol. 36, no. 10, pp. 11288–11297, Oct. 2021.

Virendra Prasad Maurya (Student Member, IEEE) received the B.Tech. degree in electrical engineering from J.S.S. Noida, Noida, India, in 2014, and the M.Tech. degree in electrical engineering, specialization in power electronics and machine drives, from the National Institute of Technology Durgapur, Durgapur, India, in 2019. He is currently working toward the Ph.D. degree in electric vehicle chargers with the Department of Electrical Engineering, Indian Institute of Technology (Banaras Hindu University), Varanasi, India.

His research interests include electric vehicle charging and the motoring drive, V2V, V2G, bidirectional power converters, and control of power electronics converters.

Rajeev Kumar Singh (Senior Member, IEEE) received the B.Tech. degree in electrical engineering from the College of Technology, Pantnagar, Pantnagar, India, in 2001, the M.Tech. degree in electrical machines and drives from the Indian Institute of Technology (Banaras Hindu University) Varanasi, Varanasi, India, in 2003, and the Ph.D. degree in electrical engineering from the Indian Institute of Technology Kanpur, Kanpur, India, in 2013.

He is currently an Associate Professor with the Department of Electrical Engineering and Associate Dean (Academic Affairs)-UG with the Indian Institute of Technology (Banaras Hindu University) Varanasi. His research interests include renewable power conversion for hybrid microgrids, power conversion for electric vehicles/hybrid electric vehicles, optimal charging/discharging of energy storage systems, and converter modeling and control.

Dr. Singh was the recipient of the Shyama Varshney BENCO-64 Best Educator Award by IIT (BHU) Varanasi in 2021.